

Contents lists available at [ScienceDirect](https://www.sciencedirect.com)

Journal of Sound and Vibration

journal homepage: www.elsevier.com/locate/jsvi

Acoustic scattering in a small centrifugal compressor based on the use of linearized equations in a rotating frame

Stefan Jacob^{a,b,*}, Emelie Trigell^b, Mihai Mihaescu^b, Mats Åbom^b^a Leibniz Institute for Solid State and Materials Research, Helmholtzstrasse 4, Dresden, Germany^b Department of Mechanics, KTH Royal Institute of Technology, Teknikringen 8, Stockholm 100 44, Sweden

A B S T R A C T

Numerical solutions of acoustic wave scattering are often used to describe sound propagation through complex geometries. For cases with flow, various forms of the convected equation have been used. A better alternative that includes vortex-sound interaction is instead to use the linearized and harmonic forms of the unsteady fluid flow governing equations. In this paper, a formulation of the linearized equations that include rotational effects, in an acoustic computation using a rotating frame of reference in a stationary geometry, is presented. We demonstrate that rotational effects can be important, e.g., when computing the transmission loss through high-speed compressors. The implementation of the proposed addition to the existing schemes is both simple and numerically inexpensive. The results are expected to have an impact on the research and development related to noise control of high-performance turbo-machinery, e.g., used in automotive or aviation applications at operating conditions that can be represented by steady background flows.

1. Introduction

The equations for compressible fluid flow, i.e., the conservation of mass and energy and the Navier-Stokes Equation are the appropriate models for fluid dynamics. They also govern the physics of sound, such as fluid-borne acoustic wave propagation, flow-acoustic interactions or vortex-sound, and flow-acoustic sources [1]. Numerical setups are the preferred strategies for solving these coupled differential equations for different applications, including aeroacoustics. Differences in the scales of the acoustic phenomena often require the use of hybrid acoustic computations that decouple the acoustic sources and the propagation. The latter, in particular the scattering of sound waves through rotating frames, is the topic of this study.

To compute sound scattering, we generally assume that the acoustic fluctuations are small compared to their mean values. The equations of motion can then be linearized and still retain the convection, propagation, and coupling of acoustic, vorticity, and entropy modes. This method is used to predict flow-acoustic and thermo-acoustic instabilities [2–4], and sound generation and propagation through fan rotor-stator configurations [5–8].

In the present work, we will focus on the scattering of sound from rotating domains. We confirm with experiments and numerical computations that the effects of rotation are important, e.g., when predictions are made regarding the acoustic transmission through an automotive compressor at relevant rotational speeds. Most of the existing methods to describe sound scattering through small, e.g., automotive compressors are low dimensional (0D or 1D [9]). In contrast, we address the problem of sound scattering through small compressors for the first time using three-dimensional numerical models. So far, three-dimensional (CFD) models have been successfully used only to study the compressor's performance and efficiency as well as its sound generation ([10–13]). However, such

* Corresponding author at: PTB, National Metrology Institute of the Federal Republic of Germany, Bundesallee 100, 38116 Brunswick
 E-mail addresses: stefan.jacob@ptb.de (S. Jacob), etrigell@mech.kth.se (E. Trigell), mihai@mech.kth.se (M. Mihaescu), matsabom@kth.se (M. Åbom).

<https://doi.org/10.1016/j.jsv.2022.117315>

Received 21 November 2021; Received in revised form 31 August 2022; Accepted 18 September 2022

Available online 20 September 2022

0022-460X/© 2022 The Authors. Published by Elsevier Ltd. This is an open access article under the CC BY-NC-ND license (<http://creativecommons.org/licenses/by-nc-nd/4.0/>).

compressors mainly operate in the low-frequency (plane wave) range and the acoustic installation effects can be large. Hence, also knowledge of the scattering properties is required to build an acoustic model of the system and minimize the noise emission.

A typical model for this problem, used by the industry, is described by Veloso et al. [14]. For the case of sound scattering through automotive turbochargers, a one-dimensional form of the complete fluid mechanical equations is solved, but without considering the effects of the rotation. This was despite that already Peat et al. [15] had earlier studied the rotational effects for automotive turbochargers, using a 1D fluid flow model. Their model was accurate for low frequencies that are dominated by the volume effects, but started to diverge largely for frequencies higher than about 30% of the first cut-on frequency. The effect of the rotation on the sound scattering was small, which they attributed to the low rotational speed (58,000 rpm) in their experiments. A recent example of acoustic scattering including the effects of rotation is a study by Foulquié et al. [16]. The authors computed rotor-stator interaction for an aero-engine fan stage by solving the Linearized Euler Equations. They explicitly account for the movement of the rotor-stage using a sliding discretization mesh methodology on a two-dimensional geometry in the time domain.

In contrast, we propose to include the effects of rotational domains by adding rotating advection of mass, momentum, and entropy to the equations of motion and a Coriolis force source-term to the Navier Stokes equation in inertial coordinates. The equations are derived referring to a formulation that is often called a “Moving Reference Frame” (MRF) in Reynold Averaged Navier-Stokes Equations (RANS), commonly used by researchers and engineers to efficiently predict flow-performance curves of rotating machinery [17–20]. Although all domains are stationary during the computation, the advective terms in the rotational parts of the geometry are recast to account for the effects of rotational motion. Furthermore, we show that these equations can be linearized for the acoustic state variables, which constitutes a new “Acoustic Moving Reference Frame” formulation of the Linearize-Navier-Stokes-Equations (LNSE) in the frequency domain. The derived formulation simplifies the numerical setups compared to Foulquié’s work [16], as it only requires a stationary, non-sliding discretization mesh. Hence, the proposed method is computationally less demanding, but recasting the equations into a time-harmonic form restricts the solutions to time-invariant systems. In this study, we present numerical solutions of the new formulation of the equations, which are validated with *in-situ* acoustic experiments covering the plane wave range on a fast spinning turbocharger compressor stage. Using two-port theory [21] a linear filter is defined and applied to the experimental data to separate anechoic far-field acoustic signals from acoustic resonances and hydrodynamic modes in the compressor flow. This method has been validated across different aeroacoustic applications and was used to quantify turbocharger compressor noise in the past [22].

2. Methods

2.1. Linearized equations of motion in a rotating frame

The purpose of the following derivation is to present the acoustic conservation equations in a rotating frame of reference. The frame is boxed in a stationary geometry where the acoustic field is described in terms of inertial coordinates. The equations in the rotating frame are also expressed in inertial variables, while the temporal derivatives are expressed relative to the rotating system. This formulation is consistent with the approach used in common fluid dynamic solvers for moving reference frames [23,24]. In Fig. 1, a principle sketch of a rotor spinning with the angular velocity Ω is presented. The velocity vector relative to the rotating frame is \mathbf{u}_r , the inertial velocity vector is \mathbf{u}_{in} , and $\mathbf{u}_r = \mathbf{u}_{in} - \Omega \times \mathbf{r}$, with $\Omega = [\Omega_x \ \Omega_y \ \Omega_z]^T$ is the angular rotation and the superscript T means the vector transpose.

The equations of fluid flow in the rotating frame, expressed in rotating variables and temporal derivatives in rotating terms are [25, 26]

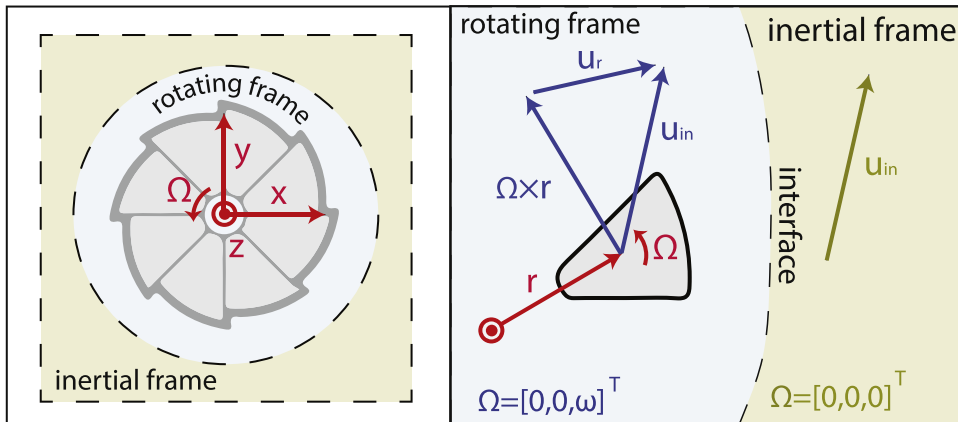


Fig. 1. Left: The rotating frame, boxed into a stationary geometry. The center of the inertial and the rotating frame is in the center of the rotor, which rotates around the z-axis. Right: Relation between the velocity in rotating and in inertial terms, at a point r that rotates with an angular velocity Ω .

$$\left[\frac{\partial \rho}{\partial t} \right]_r + \nabla \cdot \rho \mathbf{u}_r = 0 \quad (1a)$$

$$\rho \left[\frac{\partial \mathbf{u}_r}{\partial t} \right]_r + \rho \mathbf{u}_r \cdot \nabla \mathbf{u}_r = \nabla \cdot \boldsymbol{\sigma}_r + \mathbf{F}_r - \underbrace{2\rho \boldsymbol{\Omega} \times \mathbf{u}_r}_{\text{Coriolis force}} - \underbrace{\rho \boldsymbol{\Omega} \times (\boldsymbol{\Omega} \times \mathbf{r})}_{\text{Centrifugal force}} \quad (1b)$$

$$\rho T \left[\frac{\partial s}{\partial t} \right]_r + \rho T \mathbf{u}_r \cdot \nabla s = \nabla \cdot k \nabla T + \varnothing_r + S_h \quad (1c)$$

$$\text{and } \rho T ds = \rho c_p dT - \alpha_p T dp \quad (1d)$$

with the density ρ , the pressure p , the velocity $\mathbf{u} = [u_x \ u_y \ u_z]^T$, the entropy s , the temperature T , the viscous dissipation function $\varnothing_r = \nabla \mathbf{u}_r : \boldsymbol{\tau}_r$, the viscous stress tensor $\boldsymbol{\tau}$, the total stress tensor $\boldsymbol{\sigma}$, the coefficient of thermal expansion α_p , the specific heat capacity at constant pressure c_p , and the thermal conductivity k . \mathbf{F}_r and S_h are source terms for the momentum and energy equation, respectively. Note that \varnothing_r is independent of if it is calculated in the inertial or relative frame, see [Appendix A](#). The index $(\dots)_r$ indicates quantities with respect to the rotating frame and $\left[\frac{\partial}{\partial t} \right]_r$ is the temporal derivative in rotating coordinates. The operator “:” means a double contraction of the tensor product. The viscous and total stresses are defined as

$$\boldsymbol{\tau}_r = \mu (\nabla \mathbf{u}_r + (\nabla \mathbf{u}_r)^T) + \left(\mu_b - \frac{2}{3} \mu \right) (\nabla \cdot \mathbf{u}_r) \mathbf{I} \quad (2a)$$

$$\boldsymbol{\sigma}_r = -p \mathbf{I} + \boldsymbol{\tau}_r \quad (2b)$$

and μ is the shear viscosity, μ_b is the bulk viscosity, and \mathbf{I} is the identity matrix.

[Eqs. \(1a\)-\(1c\)](#) can be expressed in terms of inertial variables and temporal derivatives in the rotating frame (see [Appendix A](#))

$$\left[\frac{\partial \rho}{\partial t} \right]_r + \nabla \cdot \rho \mathbf{u}_{in} \underbrace{- (\boldsymbol{\Omega} \times \mathbf{r}) \cdot \nabla \rho}_{\text{rot. advection of density}} = 0 \quad (3a)$$

$$\rho \left[\frac{\partial \mathbf{u}_{in}}{\partial t} \right]_r + \rho \mathbf{u}_{in} \cdot \nabla \mathbf{u}_{in} \underbrace{- \rho (\boldsymbol{\Omega} \times \mathbf{r}) \cdot \nabla \mathbf{u}_{in}}_{\text{rot. advection of momentum}} = \nabla \cdot \boldsymbol{\sigma}_{in} + \mathbf{F}_r \underbrace{- \rho \boldsymbol{\Omega} \times \mathbf{u}_{in}}_{\text{Coriolis force contribution}} \quad (3b)$$

$$\rho T \left[\frac{\partial s}{\partial t} \right]_r + \rho T \mathbf{u}_{in} \cdot \nabla s \underbrace{- \rho T (\boldsymbol{\Omega} \times \mathbf{r}) \cdot \nabla s}_{\text{rot. advection of entropy}} = \nabla \cdot k \nabla T + \varnothing_{in} + S_h \quad (3c)$$

It is important to note, that although [Eqs. \(3a\)-\(3c\)](#) are expressed in inertial variables, the rotation is accounted for through the rotational advection terms, the Coriolis contribution to the momentum equation, and the temporal derivative with respect to the rotating frame. To model linear acoustic propagation small perturbations $\epsilon \ll 1$ are now assumed around a steady-state (0). This implies that

$$\mathbf{u}_{in} = \mathbf{u}_{in0} + \epsilon \mathbf{u}'_{in} + \mathcal{O}(\epsilon^2) \quad (4a)$$

$$p = p_0 + \epsilon p' + \mathcal{O}(\epsilon^2) \quad (4b)$$

$$\rho = \rho_0 + \epsilon \rho' + \mathcal{O}(\epsilon^2) \quad (4c)$$

$$T = T_0 + \epsilon T' + \mathcal{O}(\epsilon^2) \quad (4d)$$

which when inserted in [Eqs. \(3a\)-\(3c\)](#) and using [Eq. \(1d\)](#) yields

$$\left[\frac{\partial \rho'}{\partial t} \right]_r + \mathbf{u}'_{in} \cdot \nabla \rho_0 + \rho_0 \nabla \cdot \mathbf{u}'_{in} + \mathbf{u}_{in0} \cdot \nabla \rho' + \rho' \nabla \cdot \mathbf{u}_{in0} - (\boldsymbol{\Omega} \times \mathbf{r}) \cdot \nabla \rho' = 0 \quad (5a)$$

$$\begin{aligned} \rho_0 \left(\left[\frac{\partial \mathbf{u}'_{in}}{\partial t} \right]_r + \mathbf{u}'_{in} \cdot \nabla \mathbf{u}_{in0} + \mathbf{u}_{in0} \cdot \nabla \mathbf{u}'_{in} - (\boldsymbol{\Omega} \times \mathbf{r}) \cdot \nabla \mathbf{u}'_{in} \right) + \rho' (\mathbf{u}_{in0} \cdot \nabla \mathbf{u}_{in0} - (\boldsymbol{\Omega} \times \mathbf{r}) \cdot \nabla \mathbf{u}_{in0}) \\ = \nabla \cdot \boldsymbol{\sigma}'_{in} - \rho_0 (\boldsymbol{\Omega} \times \mathbf{u}'_{in}) - \rho' (\boldsymbol{\Omega} \times \mathbf{u}_{in0}) + \mathbf{F}'_{in} \end{aligned} \quad (5b)$$

$$\begin{aligned}
& c_p \rho_0 \left(\left[\frac{\partial T'}{\partial t} \right]_r + \mathbf{u}'_{in} \cdot \nabla T_0 + \mathbf{u}_{in0} \cdot \nabla T' - (\boldsymbol{\Omega} \times \mathbf{r}) \cdot \nabla T' \right) \\
& + c_p \rho' (\mathbf{u}_{in0} \cdot \nabla T_0 - (\boldsymbol{\Omega} \times \mathbf{r}) \cdot \nabla T_0) \\
& - \alpha_p T_0 \left(\left[\frac{\partial p'}{\partial t} \right]_r + \mathbf{u}_{in0} \cdot \nabla p' + \mathbf{u}'_{in} \cdot \nabla p_0 - (\boldsymbol{\Omega} \times \mathbf{r}) \cdot \nabla p' \right) \\
& - \alpha_p T' (\mathbf{u}_{in0} \cdot \nabla p_0 - (\boldsymbol{\Omega} \times \mathbf{r}) \cdot \nabla p_0) = \nabla \cdot (k_{th} \nabla T') + S'_h + \hat{\mathcal{O}}'_{in}
\end{aligned} \tag{5c}$$

Here, the prime symbol indicates a first-order acoustic perturbation, and the index 0 indicates the steady background mean flow. In formulating Eq. (5c) the thermodynamic relation 1d has also been used. Note that \mathbf{u}_{i0} and \mathbf{u}_{r0} contain all the steady velocity components and that $\mathbf{u}_{in} = \mathbf{u}_r + \boldsymbol{\Omega} \times \mathbf{r}$, and therefore $\mathbf{u}'_{in} = \mathbf{u}'_r = \mathbf{u}'$.

Eqs. (5a)-(5c) are the linear form of the equations of fluid flow, in which the time derivative is expressed in terms of rotating coordinates and the dependent variables are expressed in the inertial frame. For $\boldsymbol{\Omega} = 0$, the equations transform to the ordinary linearized Navier-Stokes equations. Rotating domains can be included in geometries by defining $\boldsymbol{\Omega} \neq 0$ in the rotating domain and $\boldsymbol{\Omega} = 0$ in the remaining geometry, as indicated in Fig. 1.

Eqs. (5a)-(5c) can be further simplified by assuming time-harmonic solutions of the acoustic state variables, i.e. the acoustic fields are expressed in a complex form as $p' = \hat{p} e^{i\omega t}$, $\rho' = \hat{\rho} e^{i\omega t}$, $T' = \hat{T} e^{i\omega t}$, $\mathbf{u}' = \hat{\mathbf{u}} e^{i\omega t}$. The hat symbol indicates the complex-valued amplitude of the harmonic acoustic state variable, ω is the angular frequency, and $i = \sqrt{-1}$. This yields

$$i\omega \hat{p} + \hat{\mathbf{u}} \cdot \nabla \rho_0 + \rho_0 \nabla \cdot \hat{\mathbf{u}} + \mathbf{u}_{in0} \cdot \nabla \hat{p} + \hat{p} \nabla \cdot \mathbf{u}_{in0} - (\boldsymbol{\Omega} \times \mathbf{r}) \cdot \nabla \hat{p} = 0 \tag{6a}$$

$$\rho_0 (i\omega \hat{\mathbf{u}} + \hat{\mathbf{u}} \cdot \nabla \mathbf{u}_{in} + \mathbf{u}_{in0} \cdot \nabla \hat{\mathbf{u}} - (\boldsymbol{\Omega} \times \mathbf{r}) \cdot \nabla \hat{\mathbf{u}}) + \hat{p} (\mathbf{u}_{in} \cdot \nabla \mathbf{u}_{in0} - (\boldsymbol{\Omega} \times \mathbf{r}) \cdot \nabla \mathbf{u}_{in0}) = \nabla \cdot \hat{\boldsymbol{\sigma}}_{in} - \rho_0 (\boldsymbol{\Omega} \times \hat{\mathbf{u}}) - \hat{\rho} (\boldsymbol{\Omega} \times \mathbf{u}_{in0}) + \hat{\mathbf{F}}_{in} \tag{6b}$$

$$\begin{aligned}
& c_p \rho_0 (i\omega \hat{T} + \hat{\mathbf{u}} \cdot \nabla T_0 + \mathbf{u}_{in0} \cdot \nabla \hat{T} - (\boldsymbol{\Omega} \times \mathbf{r}) \cdot \nabla \hat{T}) + c_p \hat{p} (\mathbf{u}_{in0} \cdot \nabla T_0 - (\boldsymbol{\Omega} \times \mathbf{r}) \cdot \nabla T_0) - \alpha_p T_0 (i\omega \hat{p} + \mathbf{u}_{in0} \cdot \nabla \hat{p} + \hat{\mathbf{u}} \cdot \nabla p_0 \\
& - (\boldsymbol{\Omega} \times \mathbf{r}) \cdot \nabla \hat{p}) - \alpha_p \hat{T} (\mathbf{u}_{in0} \cdot \nabla p_0 - (\boldsymbol{\Omega} \times \mathbf{r}) \cdot \nabla p_0) = \nabla \cdot (k_{th} \nabla \hat{T}) + \hat{\mathcal{O}}_{in} + \hat{S}_h
\end{aligned} \tag{6c}$$

With

$$\nabla \cdot \hat{\boldsymbol{\sigma}} = -\nabla \hat{p} + \nabla \cdot \hat{\boldsymbol{\tau}} \tag{6d}$$

$$\hat{\boldsymbol{\tau}} = \mu (\nabla \hat{\mathbf{u}} + (\nabla \hat{\mathbf{u}})^T) + \left(\mu_b - \frac{2}{3} \mu \right) (\nabla \cdot \hat{\mathbf{u}}) \mathbf{I} \tag{6e}$$

$$\hat{\mathcal{O}}_{in} = \nabla \hat{\mathbf{u}} : \boldsymbol{\tau}_{in0} + \nabla \mathbf{u}_{in0} : \hat{\boldsymbol{\tau}} \tag{6f}$$

Eqs. (6a)-(6c) are the linearized and time-harmonic equations of fluid flow. They include the effect of rotation on the fundamental equations, but the solutions are time-invariant. Time-invariant models are commonly used in flow duct acoustics (e.g. [27–30]). Also, common low-dimensional models for small compressors (e.g. Veloso et al. [14], and Peat et al. [15]) assume time-invariance. The problem can be further simplified, if time variations of the geometry are neglected. In this case, the sound scattering can be computed for a single rotor position only, leading to a very efficient computational model with a stationary mesh, containing the inertial and rotating frames. This is in line with the “moving reference frame” used in fluid dynamics [31].

We would like to note, that the effects of viscosity and thermal conduction are included, but the presented procedure is also valid for simpler fluid models. For example, setting the viscosities to zero would result in the Linearized Euler Equations in a rotating frame.

2.2. Acoustic mode decomposition and scattering matrix

The automotive compressor that we investigated in this study required special inlet and outlet treatments in the experiments, that could not be translated directly into the numerical domain. The acoustic reflections at the inlet and outlet terminations in the experiments differ from the numerical simulations. Therefore, the results in this paper are processed with an acoustic mode decomposition technique and present the ratio of complex-valued amplitudes of the aeroacoustic duct modes that propagate in the inlet and outlet pipes of the compressors. This technique allows us to separate reflected and transmitted wave components and to remove the effect of boundary reflections as well as uncorrelated sources from the data. For the case studied the only propagating mode is the plane wave and reflection/scattering can be described by a two-port scattering matrix [21]. During decomposition, the simulated or measured pressure fields are projected on the plane wave mode. With an inverse method based on least-squares, the amplitudes and phases of the waves are extracted. The method is explained in detail in our previous works [32,33] and is summarized below.

Let us assume acoustic modes of the general shape $p'_m = \hat{p}_m \Psi_m e^{-ik_m z}$. Here \hat{p}_m and Ψ_m are the complex-valued amplitude and the complex-valued shape of the m -th mode, respectively, and k_m represent the wavenumbers and z the coordinate along the duct axis. At a given frequency, only a finite set of modes will propagate, which are called “cut-on modes”. For the frequencies considered in this study (300 – 3300 Hz), only the planar acoustic modes were cut-on modes, so that $m = \pm 1$ and \pm indicate the direction of the propagating wave in the positive and negative directions. Mode shapes can show a slight dependency on the flow profiles caused by convection and refraction in the background flow [34]. We did not consider this effect in the study and assumed $\Psi_{1+} = \Psi_{1-} = 1$. The effect of flow is

stronger on the phase velocity of the modes; thus, the wavenumbers are corrected for convection and thermo-viscous effects using $k_{1\pm} = \pm \frac{\omega}{c} k_{0\pm}$ where $k_{0\pm}$ is a complex valued correction factor [35,36]. The linear acoustic theory leads to a formulation for the harmonic pressure at an arbitrary point along the experimental or numerical duct or in the numerical grid with the longitudinal coordinate z_j

$$p'_j = \hat{p}_+ e^{-ik_+ z_j} + \hat{p}_- e^{ik_- z_j}. \tag{7}$$

The index $(\dots)_j$ refers to the j -th measurement point and the indices $(\dots)_1$ denoting the mode order was dropped for convenience. Eq. (7) contains the two unknown frequency-dependent complex-valued pressure amplitudes of the upstream (-) and downstream (+) propagating modes. Sampling the pressure field at more than two points along the ducts leads to an overdetermined linear algebraic system that can be solved for the mode amplitudes. In this paper, the system of equations was solved using a generalized Moore-Penrose inverse [37].

Assume that the four complex-valued plane-wave amplitudes that propagate away (\hat{p}_+^i and \hat{p}_+^o) and towards (\hat{p}_-^i and \hat{p}_-^o) the inlet and outlet pipe of the compressor are known at each frequency. The passive acoustic characteristics of the compressor can then be described with a frequency-dependent two-port scattering matrix S

$$S = \begin{bmatrix} \hat{p}_+^i / \hat{p}_-^i & \hat{p}_+^i / \hat{p}_-^o \\ \hat{p}_+^o / \hat{p}_-^i & \hat{p}_+^o / \hat{p}_-^o \end{bmatrix} = \begin{bmatrix} R^i & T^{o \rightarrow i} \\ T^{i \rightarrow o} & R^o \end{bmatrix}. \tag{8}$$

Here, $R^{i/o}$ is the reflection coefficient at the inlet or outlet and $T^{i \rightarrow o}$ is the transmission coefficient from the compressor inlet to the outlet or vice versa. To determine this scattering matrix numerically or experimentally two independent sets of incident waves must be created [21].

2.3. Numerical method

In the proposed method, the acoustic scattering of an automotive compressor is captured using a hybrid approach. First, the background flow ($\mathbf{u}_{in0}, T_0, \rho_0, p_0$) is solved in a finite-volume solver. Subsequently, Eqs. (6a)-(6c) are solved in a finite element solver. These procedures are detailed below.

2.3.1. Background flow

The steady background flow was computed with a compressible Reynolds-Averaged Navier-Stokes (RANS) model in the commercial finite-volume solver Star-CCM+ (version 15.02.007-dp). Here, a time-averaged version of Eqs. (3a)-(3c) was solved using an SST (Menter) K-Omega turbulence model to describe the turbulent stresses [38]. During the computation, the rotor position was fixed

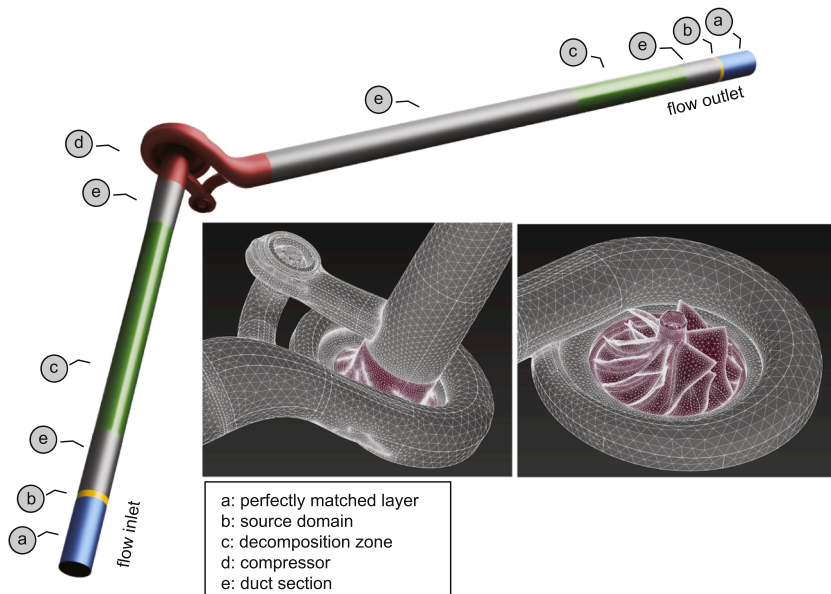


Fig. 2. Sketch of the numerical domain. The setup corresponds to the experiments (Fig. 3), whereas the acoustic absorbers (or mufflers) are replaced by perfectly matched layers (a), the loudspeaker sources by source domains (b), and microphone arrays by decomposition zones (c). Duct sections close to the external sources and the compressor are not used for the acoustic decomposition (e). The plots of the meshes contain the non-rotating domain (gray) and the rotating domain (purple). The rotation domain had increased mesh density, with elements as small as 300 μm . (For interpretation of the references to colour in this figure legend, the reader is referred to the web version of this article.)

and a steady flow field for that rotor position was computed, including the effect of rotation in the solved equations. The effect of rotation is captured using a moving reference frame. A mixing plane interface is applied to circumferentially average the coupling between the rotating and the inertial domain. This model has been successfully used in several studies on rotational machinery, and the influence of the rotor position on the results is usually low [13,39,10]. Because background flow computations are well established, we only provided a summary of the main geometrical setup and the boundary conditions. Details related to background flow computations can be found in the literature mentioned above.

The computational domain contained the full geometry adopted from the manufacturing CAD drawings without simplification, namely, an impeller with six main blades and six splitter blades, a vane-less diffuser, a compressor volute, and a recirculation valve. Inlet and outlet pipes were extended to a length of 0.5 m and 1 m, respectively. The inlet and outlet pipe radii were 22 mm and 27.5 mm, respectively. The geometry was discretized with a polyhedral mesh with 4 million cells between 17 μm and 1.7 mm in size; 60% of the cells were clustered in the impeller region. Inlet and outlet pipes contained a structured grid that stretched towards the terminations. Additionally, a prismatic boundary-layer mesh with eight layers was generated, resolving the viscous boundary layers with a y^+ value close to unity. The following boundary conditions were defined: mass flow rate at the inlet, outlet total pressure, no-slip ($u|_{\text{wall}} = 0$) adiabatic walls, and air as an ideal gas with the properties: $T_0 = 299$ K, $P_0 = 101.325$ Pa, $\mu_{\text{dyn}} = 1.85508E - 5$ Pa s, $\rho_0 = 1.166 \frac{\text{kg}}{\text{m}^3}$ (surface averaged) at the inlet of the compressor.

2.3.2. Acoustic scattering

A principle sketch of the finite element domain for acoustic scattering is shown in Fig. 2. It contains the compressor geometry adopted from a production drawing CAD without simplification (identical to the geometry used for the background flow). In addition, the figure shows the extended pipe section with 22mm and 27.5mm radius at the inlet and outlet, respectively, source regions, and terminating acoustic absorber domains (Perfectly Matched Layers). Parts of the extended pipes at the inlet and the outlet were used as ‘‘Decomposition Zones’’, i.e., regions where the pressure was sampled for post-processing in order to compute the scattering matrix. The purple area in the mesh plot shows the domain that was used as the rotating frame. It was centered and aligned with the rotor axis and included the complete impeller, running through half the tip-clearance gap between the impeller and cut-off region to host the rotational domain. The domain was modeled in the commercial the finite element solver Comsol Multiphysics v. 5.5 [40] and discretized with unstructured, tetrahedral elements with a maximum size of 6 mm (20 elements per smallest wavelength) in the inlet pipe and a minimum size of 300 μm inside the compressor and situated near to the compressor blades and the clearance. Additionally, the visco-thermal boundary (Stokes) layers were resolved with a hexahedral boundary layer mesh. This resulted in a mesh with 1.3 million elements.

The tangential acoustic velocity at the walls was constrained to zero (‘‘no-slip’’ condition). For comparison, we computed a test case with the normal velocity constrained to zero (‘‘slip’’ condition) in the rotating frame. The results did not show a noticeable difference which indicates that the boundary layer losses in the rotating frame are low.

The acoustic computations and the background flow computations were performed on separate discretization schemes. Therefore, the background flow field had to be interpolated on the acoustic grid points. Although this interpolation is pointwise correct, the shape functions of the finite elements are not necessarily smooth. This leads to unphysically large gradients which are a source of numerical instabilities. To reduce instabilities, artificial diffusion was added to the interpolation

$$-\nabla \cdot (D_{LNSE} \nabla b_{LNSE}) + b_{LNSE} = b_{RANS} , \quad (9)$$

where b is the interpolated quantity and D_{LNSE} is the diffusivity. The parameter b_{LNSE} is the field used in the acoustic computation and b_{RANS} is the background field, linearly interpolated on the coordinates of the acoustic grid. This strategy is recommended by the commercial FEM software Comsol Multiphysics, which was used in this study [40]. Here, a diffusivity that depends on the size of the numerical grid elements is used, e.g. $D = h^2 k$, where h is the dimension of the grid element and k is the diffusivity constant. The value was determined iteratively, starting from a small value (10^{-4}) that was subsequently increased until the solution got stable. As a criterion for stability, the smoothness of the sound scattering coefficient over frequency was examined. We found that the solution stabilized for values of $k > 0.01$, which is the recommendation in Ref. [40].

Eqs. (6a)-(6c) are defined in a weak form and $\Omega = [0 \ 0 \ 10051 \text{rad/s}]^T$ is set inside the rotational domain and $\Omega = [0 \ 0 \ 0]^T$ in the remaining geometry. The angular frequency 10,051 rad/s corresponds to 96,000 RPM. Furthermore, harmonic forces were added in the axial direction at the source domains in the inlet or outlet pipes ($F_{axial}^i = 1e^{i\omega t}$) to create two test cases for the determination of the scattering matrix. The amplitude of the force is arbitrary because the equations are linear and the value 1 was chosen for simplicity. If the excitation of non-planar modes is intended, the amplitude must be in the shape of the excited mode [33]. Here a constant value over the cross-section was used to excite plane waves.

At the nodes at the interfaces between the inertial and the rotating frame, we imposed continuity on the dependent variables. We considered a single position of the rotor, for which we computed two sets of solutions with upstream and downstream sources enabled, respectively. Eqs. (6a)-(6c) were solved for a discrete set of excitation frequencies (from 300 to 3300 Hz in steps of 20 Hz), resulting in a total of 2×150 computations. The equations were solved using the commercial FEM Solver Comsol Multiphysics (version 5.6) with the Multifrontal Massively Parallel Sparse Direct Solver (MUMPS [41, 42]), running on a high-performance cluster in parallel on 8 nodes

(2×12 Intel E5–2690v3 Haswell cores, 512 GB RAM).¹ The entire acoustic computation with this setup took 3 h (=576 CPUh). The pressure field was acquired in the decomposition zones on which acoustic mode decomposition was performed using the Python package Acdecom [43].

2.4. Validation data

Experimental validation data was measured in the aeroacoustic test facilities at KTH's Competence Center for Gas Exchange.² A principle sketch of the measurement set up is shown in Fig. 3. Only the compressor side is shown, but the turbine was mounted during the experiment to operate the compressor. The turbine was connected through a set of flexible pipes to a pressurized and preheated (120 °C) air supply. The operation conditions of the turbocharger were then controlled by adjusting the mass flow rate through the turbine and the pressure at the compressor outlet, while the rotational speed of the compressor was monitored using an electromagnetic sensor (type Micro-epsilon turboSPEED 135) flush-mounted to the scroll.

The validation experiment involved the following steps:

- 1 The operation point was adjusted and the compressor was operated until a stable temperature and rotation were achieved. All the equipment located at the outlet side of the compressor was water-cooled during the operation.
- 2 During stable operation, acoustic excitation from the loudspeaker sources at the inlet and outlet sides were enabled. The sources were used simultaneously with a total of eight loudspeakers (four upstream and four downstream), with eight sinusoidal signals at eight different frequencies. We recorded the unsteady pressure field with three microphones at the inlet and three microphones at the outlet side. From the pressure fields at the microphones, the transfer functions between the microphones and the loudspeakers were computed using 30 averages on spectra with a resolution of 1 Hz. This resulted in 48 (6×8) spectra for each set of test frequencies.
- 3 Subsequently, a predefined discrete set of excitation frequencies was measured, from 300 Hz to 3300 Hz in steps of 10 Hz. This procedure typically took around six hours.
- 4 The data were post-processed using the wave decomposition method and the transfer coefficients were computed, see Eq. (8). The postprocessing was done in Python 3.9 with the Acdecom package [43].

In a final step to reduce random errors, the coefficients were expressed as finite impulse response (FIR) filters. To this end, the scattering coefficients were transformed into a linear constant-coefficient difference form, using a z-transform, and the poles and zeros of the filter were estimated with Levi's method [44].

3. Results

We present results concerning the numerical computation of acoustic scattering in a rotating domain using a new formulation of the linearized Navier-Stokes equations. We found that the effect of the rotation on sound scattering is important when tested on an automotive air compressor under design conditions at around 10^5 revolutions per minute. Rotation was added in the form of advected mass, momentum, and entropy, as shown in Eqs. (6a)-(6c). This gave rise to sources in the vicinity of the blades that influence the transmission of sound waves through the compressor.

3.1. Operating conditions for the air compressor

The operating conditions are summarized in Table 1. The values are averaged over the time of the experiment (around six hours). The mass flow rate was computed from dynamic pressure measurements and temperature in the inlet pipe using Bernoulli's principle and assuming fully developed turbulent flow. The pressure ratio was determined from inlet total pressure and outlet total pressure measurements. The value was around 10% smaller than values determined on a separate performance test rig by the manufacturer, indicating some minor leakage along the outlet transmission path. Microphones were calibrated against a reference microphone for amplitude and phase at all the measured frequencies. The uncertainties presented below are at the 95% confidence interval of the acquired data during the measurement time.

Fig. 4(a) summarizes the results of our experiments for the transmission coefficient from inlet to outlet ($i \rightarrow o$) and outlet to inlet ($o \rightarrow i$), measured in 10 Hz increments. The data exhibits pronounced noise transmission at low frequencies (300 Hz – 500 Hz) and a resonant pattern in the entire spectrum. The hydrodynamic fluctuations in the measurements were well suppressed by the two-port education procedure, resulting in coefficients with low random noise. The presented data was in accordance with earlier measurements on similar geometries [45].

We fitted an FIR filter to the transmission coefficient to smooth the experimental results. The blue lines in Fig. 4(a) represent the FIR-filter spectrum, fitted with 25 poles and 25 zeros. The filter was found to be an accurate approximator for the absolute value and the phase (not presented here) of the scattering parameters. The number of poles and zeros was determined by trial and error, starting from low values and increasing until a converged result was reached.

¹ <https://www.pdc.kth.se>

² Website of the center: <https://www.ccgex.kth.se/aboutccgex>

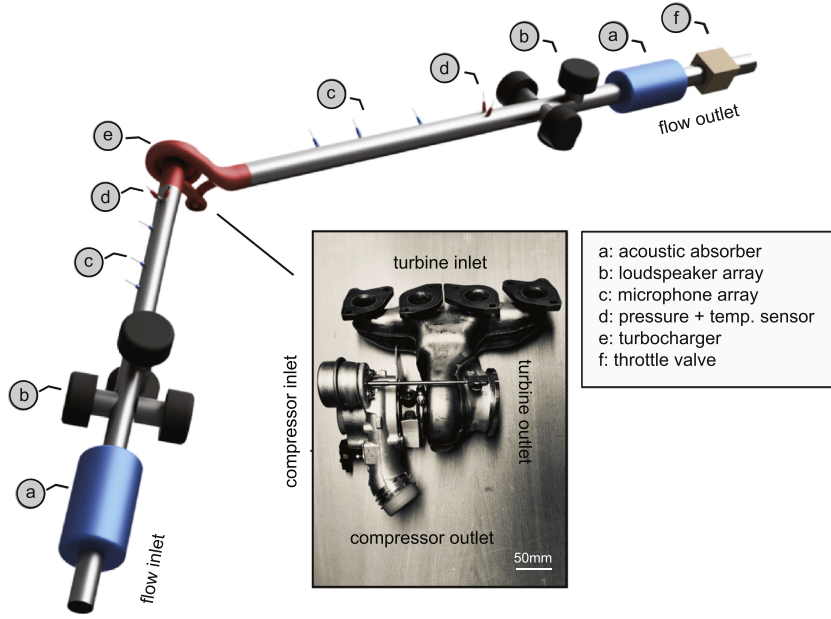


Fig. 3. Sketch of the measurement setup and a photo of the studied turbocharger, including compressor and turbine. The test setup contained extruded pipes and the equipment (a-f) needed to drive the compressor and extract the acoustic transmission coefficients with the two-port method [21]. Inlet and outlet pipe diameter were 22 mm and 27.5 mm, respectively.

Table 1

Comparison of operating conditions during the experiments and the numerical setup.

	Experiments	Simulations
Rotational Speed [RPM]	96,000 ± 2000	96,500 (input)
Massflow [kg/s]	0.12 ± 0.004	0.12 (input)
Pressure Ratio Outlet / Inlet	1.53 ± 0.02	1.64 (outlet pressure input, inlet pressure computed)
(T_{inlet}, T_{outlet}) [K]	(298, 356.1) ± 5	(299, 363.9) (input, computed)

3.2. Simulations

The results presented for the steady flow field (u_0, ρ_0, p_0 , and T_0 in Eqs. (6a)-(6c) can be used to estimate the flow performance. In Fig. 5 we present the total efficiency and the total pressure ratio between outlet and inlet, measured in a performance test rig at the supplier facilities and compared with the numerical results at the operation point (indicated with the red dot). The numerical results differ less than two percent from the measurements. We slightly overpredicted the total efficiency, whereas the pressure ratio was predicted accurately.

With the flow field as a background mean flow, we solved (1) Eqs. (6a)-(6c), and (2) the traditional linearized equations of fluid flow (i.e., with $\Omega = 0$) for comparison. We found that the implementation of the advected entropy in Eq. (6c) destabilized the numerical computations. This could be attributed to local disturbances of the numerical results in the acoustic temperature field that led to large gradients and unphysically high local energy sources caused by the term $(\Omega \times r) \cdot \nabla T'$. Therefore, we proposed and tested two simplifications of Eq. (6c) that led to stabilized numerical solutions. First, we assumed adiabatic wave propagation, which is a common assumption in linear acoustics [3]. The adiabatic assumption disables the temperature dependency in the energy equation. Second, we solved the complete Eq. (6c), but stabilized \hat{T} in the advected term adding diffusion

$$\begin{aligned}
& c_p \rho_0 (i\omega \hat{T} + \hat{\mathbf{u}} \cdot \nabla T_0 + \mathbf{u}_{in_0} \cdot \nabla \hat{T} - (\Omega \times \mathbf{r}) \cdot \nabla \hat{T}_{mod}) \\
& + c_p \hat{p} (\mathbf{u}_{in_0} \cdot \nabla T_0 - (\Omega \times \mathbf{r}) \cdot \nabla T_0) \\
& - \alpha_p T_0 (i\omega \hat{p} + \mathbf{u}_{in_0} \cdot \nabla \hat{p} + \hat{\mathbf{u}} \cdot \nabla p_0 - (\Omega \times \mathbf{r}) \cdot \nabla \hat{p}) \\
& - \alpha_p \hat{T} (\mathbf{u}_{in_0} \cdot \nabla p_0 - (\Omega \times \mathbf{r}) \cdot \nabla p_0) \\
& = \nabla \cdot (k_{th} \nabla \hat{T}) + \hat{\Phi}_{in} + \hat{S}_h
\end{aligned} \tag{10a}$$

and

$$-\nabla \cdot (D_{mod} \nabla) \hat{T}_{mod} + \hat{T}_{mod} = \hat{T}. \tag{10b}$$

Eq. (10b) was coupled to Eq. (10a) and solved in each iteration. Here, we found that a diffusivity with a constant value $D_{mod} = 0.1$

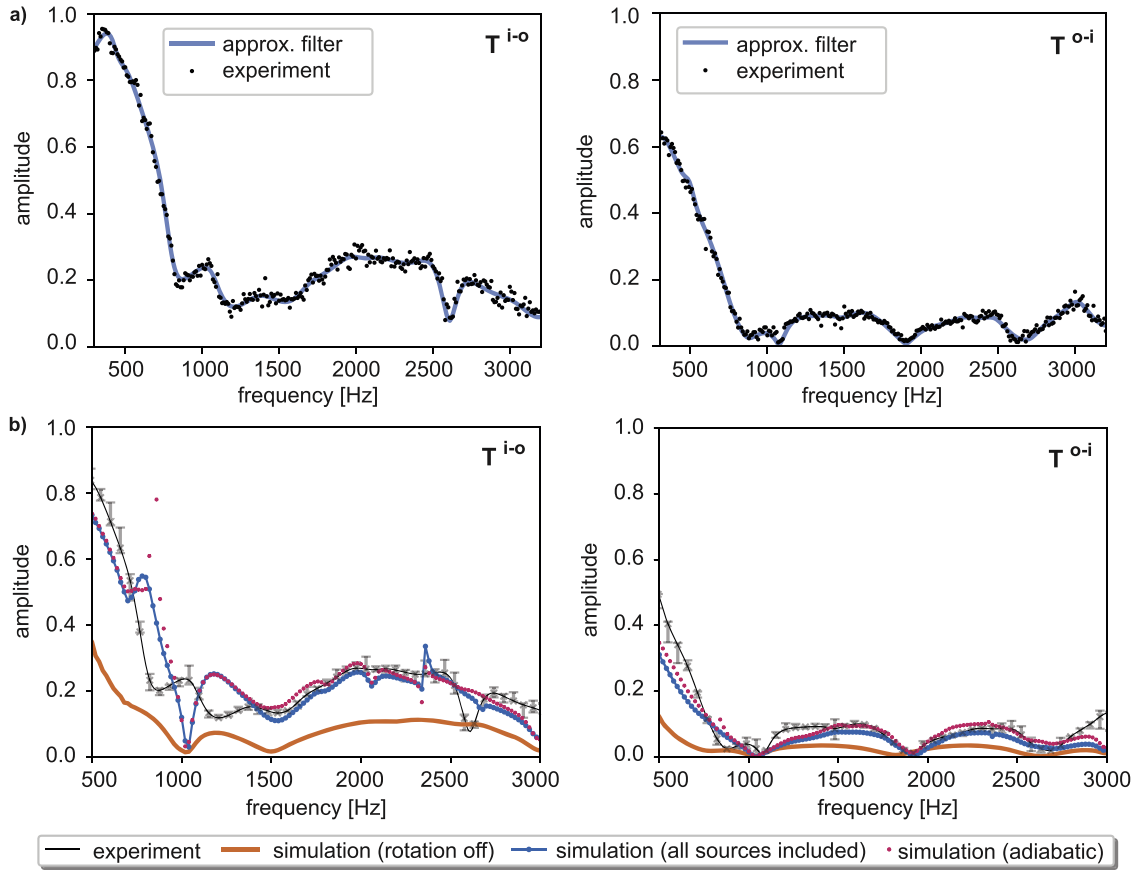


Fig. 4. (a) Transmission coefficients for the acoustic plane wave, extracted from experiments applying the two-port theory. The dots show the experimental data. The line is an approximated FIR filter acting as a smoothing function for the experiments. (b) The experimental results (black line) compared to the numerical computations using different levels of approximations. The uncertainty intervals of the measurements are the 95% intervals (2σ) estimated from a Monte Carlo method, assuming max. 5% standard deviation in temperature and pressure measurements. Solutions from the classical linearized equation (LNSE) of motion (without rotation, orange line) largely underestimate the transmission, whereas the LNSE computations including the rotating domains show significantly improved agreement. The blue line shows the simulation including all additional terms (mass, momentum, energy). The purple dots show an adiabatic assumption. Performance for inlet-outlet (i-o) transmission is similar to the performance for outlet-inlet (o-i) transmission. (For interpretation of the references to colour in this figure legend, the reader is referred to the web version of this article.)

stabilized the solution. To determine this value, we started with low values for D (10^{-13}) and subsequently, increase D until the solution became stable.

The results for the stabilized and the computation under the adiabatic assumption are presented in Fig. 4b. We compared the acoustic transmission coefficient computed with the method proposed in this paper Eqs. (6a)-(6c), the traditional linearized equations (LNSE) of motion and the validation experiments. The proposed method and the experiments revealed a good agreement, except for the upstream direction (i-o) around 1000 Hz and 2500 Hz, whereas the classical LNSE method, without rotation included, largely underestimated the transmission coefficients. Furthermore, we found that dropping the energy equation in the proposed new model and using the adiabatic assumption is a reasonable approximation.

Fig. 6 shows the source terms introduced by the addition of the rotational frame in Eqs. (6a)-(6c). We present the rotational advection of density (fluctuating part of $(\Omega \times \mathbf{r}) \cdot \nabla \rho$, Eq. (6a)), the combined rotational advection of momentum and the Coriolis contribution (fluctuating part of $\rho(\Omega \times \mathbf{r}) \cdot \nabla \mathbf{u}_{in} - \rho \Omega \times \mathbf{u}_{in}$, Eq. (6b)), and the rotational advection of entropy (fluctuating part of $T\rho(\Omega \times \mathbf{r}) \cdot \nabla s$, Eq. (6c)). We plotted their contribution at each of the discrete points in the computational grid 1500 Hz, whereas the smallest sources (smaller than 10% of the maximum sources) were omitted. This representation reveals that the most significant contributions lay in the vicinity of the blades, whereas the sources in the remaining domain are small. The advected rotational terms in the conservation of mass (Eq. (6a)) and the energy equation (Eq. (6c)) were located at the pressure side of the blades, with an increased contribution toward the blade tips. In contrast, the additional terms in the Navier-Stokes equation contributed to the suction and the pressure side of the blade. This general behavior of the result was not sensitive to the frequency studied.

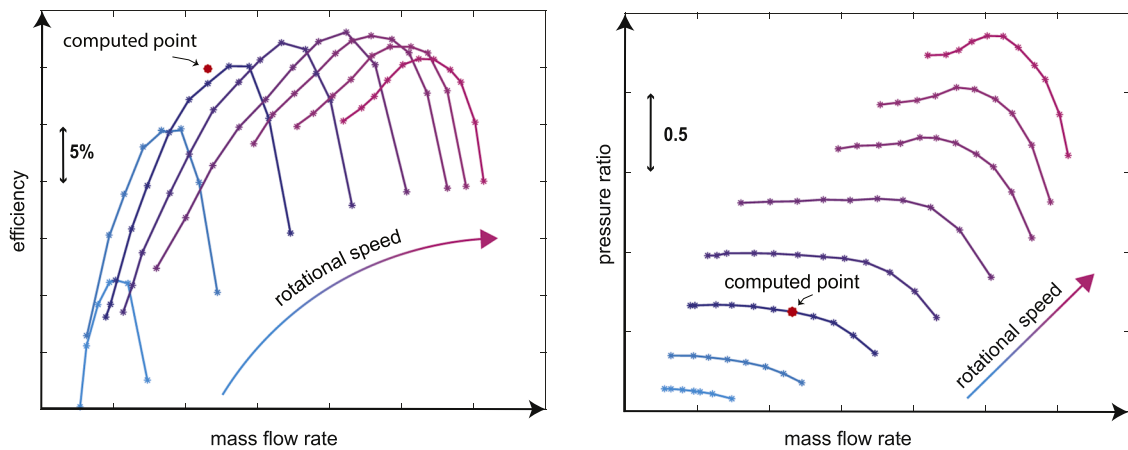


Fig. 5. The total efficiency map and total pressure ratio map of the compressor, measured at the supplier facilities. Total efficiency refers to the ratio of power output and the power input, which is based on the discharged volume and the total pressure rise. The pressure ratio refers to the ratio of total pressure at the outlet and the total pressure at the inlet. The red dots indicate the computed performance using RANS. The efficiency was overestimated by less than 2%. (For interpretation of the references to colour in this figure legend, the reader is referred to the web version of this article.)

4. Discussion and conclusion

The results in Fig. 4b imply a significant improvement of computed sound transmission when the effects of rotation in a fast-spinning domain are included in the linearized equations of fluid-flow. This finding shows that rotational effects are relevant for sound scattering from high-speed machines (tip Mach-numbers ~ 1) and should be included when such cases are investigated. The new procedure proposed facilitates a steady-state (frequency domain) formulation of the governing equation (Eqs. (6a)-(6c)) that accounts for rotational effects. This approach allows us to define a computationally efficient framework, which can be boxed into existing numerical setups. This is useful for the development of low-noise rotating machines where the plane wave range is important, e.g., compressors for IC engines or fuel cells.

The method uses a formulation of the equations of fluid motion, that is linearized in the acoustic perturbations around a steady background flow. Unsteadiness of flows in aero-engines can appear close to surge and stall operation. The compressor used in this study was operating at a design operation point during the measurements and the flow conditions are therefore stable. The good agreement between performance measurements and a steady RANS computation in Fig. 5 supports the validity of a steady flow formulation.

The rotation of the non-inertial frame contributes in the form of additional sources (see Eqs. (6a)-(6c)), especially those situated close to the rotor but not in the bulk volume (Fig. 6). The size of the rotating domain is, therefore, not very critical as long as the blades are included. The most important contribution came from the Navier-Stokes equation for the conservation of momentum (Eq. (6b)). The second most important contribution came from the conservation of mass equation (Eq. (6a)). Advected entropy had no significant effect on the results, which implies that the energy equation can be dropped and replaced by an adiabatic assumption.

Implementing Eqs. (6a)-(6c) can result in numerical instabilities for some frequencies, as described in Section 2.3.2. Instead, the computationally much less demanding and stable adiabatic assumption can be used in cases similar to the presented study. This simplification performed almost as accurately as the full implementation (Fig. 4b). However, the approach might not be physical in other applications, e.g., when acoustic heat conduction plays a relevant role.

The experimental data that was used for validation was measured for a high-speed automotive compressor at operating conditions. Care was taken to clean the experimental data from acoustic resonances in the test setup and from local, hydrodynamic pressure fluctuations that were not part of the acoustic field. To this end, the two-port theory was used, which can suppress both types of disturbances (Section 2.4). Hence, the curves presented in Fig. 4 are clean, in the sense that they represent pure acoustic transmission with boundary reflections removed. However, imperfections in the measurements, e.g., structural vibrations and differences in the geometries, can still cause uncertainties in the data. The agreement between experiments and numerical results suggests that those differences were small and did not affect the eduction of the transmission coefficients.

A possible weakness of this approach is that the model computes the acoustic scattering through the rotor at a single arbitrary position. This is done by imposing a continuity condition on the dependent variables at the nodes on the interface between the rotating and the inertial domain. The position of the rotor could affect the sound scattering. If this is suspected in a particular application, a different type of interface would be necessary. One possibility is to match the circumferential averages of the dependent variables. In fluid dynamic computations, this is sometimes referred to as the “mixing plane” approach. Another option is to repeat the numerical procedure for several rotor positions and, for example, compute an average transmission coefficient for the results. This is sometimes referred to as the “sliding mesh” approach. Using either of the options could be relevant if the wavelength of the acoustic wave is in the same dimensions as the rotor-blade distances or the volute clearance. This was not the case in the presented study, because we only examined plane waves with wavelengths that were much larger than the rotor blades. The flow field and the acoustic scattering were

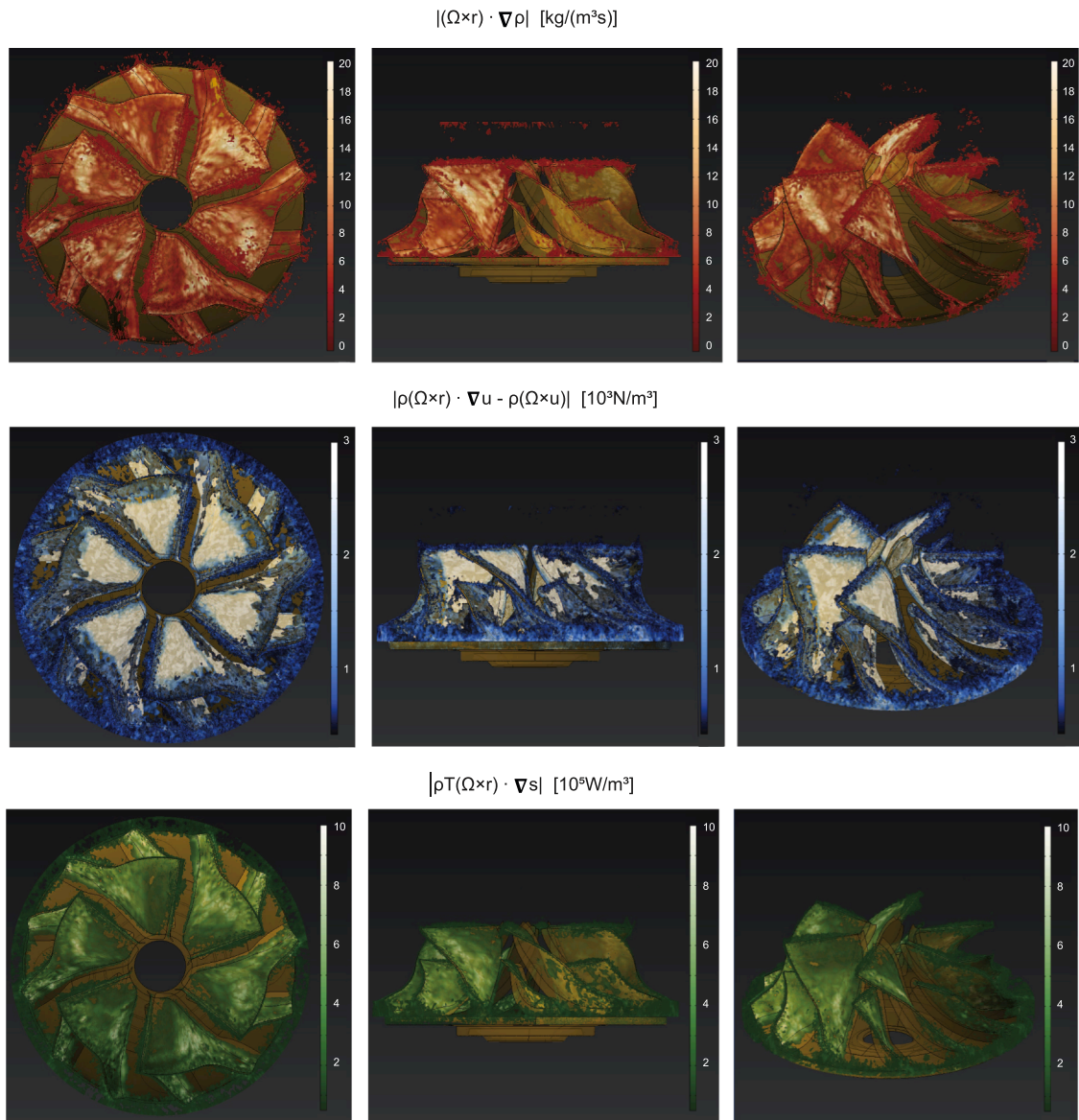


Fig. 6. Top, side, and angled view of the rotating domain. The colors show the amplitudes of the terms added by the rotation in Eqs. (6a)–(6c) at 1500 Hz. Values at the grid points of the volume are presented, whereas values smaller than 10% of the maximum value were omitted. The maximum contribution is found along with the blades. Mass and energy terms are mainly added on the pressure side, with an increased contribution towards the tips. Momentum is added on the pressure and suction side, with strong contributions towards the center of the blades.

computed for the same fixed rotor position and continuity of the dependent variables was imposed at the interface. The agreement between experiments and numerical computations suggests that this approach is sufficient for the application presented in this paper. The time-varying geometry created at the rotor and the time invariance of the involved physics can also modulate incident acoustic waves and cause a Doppler shift. This will result in a scattering of acoustic energy corresponding to multiples of the blade passing frequency. Neglecting this effect can lead to errors in the form of an energy loss at the measured frequency. This can become relevant for acoustic problems in which higher-order modes are considered. In such cases, the simplifications of time-harmonic solutions as provided in Eqs. (6a)–(6c) cannot be used and the problem must be solved in the time-domain (Eqs. (5a)–(5c)), possibly with a non-stationary mesh. The proposed frequency-domain method is, therefore, most relevant for low-frequency aero-acoustic problems, for example, to investigate acoustic scattering for small compressors.

Declaration of Competing Interest

None.

Data Availability

Data will be made available on request.

Acknowledgement

This study was conducted as part of a project within the Competence Center for Gas Exchange (CCGEx) at KTH. During this project Stefan Jacob held a post-doc position at KTH. The authors would like to acknowledge the Swedish Energy Agency, Volvo Cars, Volvo GTT, Scania, BorgWarner Turbo Systems Engineering, and Wärtsilä.

The computations were enabled by resources provided by the Swedish National Infrastructure for Computing (SNIC), PDC at KTH, partially funded by the Swedish Research Council through grant agreement no. 2018–05973.

Appendix A

Here, the derivation of the N-S equations in the rotating frame (r) expressed in inertial velocities (in) and temporal derivatives in the rotating frame is shown. These equations are commonly used for modeling rotating machines, see e.g. [46,47], and are available in commercial codes [23,24]. However, the derivation is not found in standard textbooks on fluid mechanics and the equations are also not well-known in the acoustic community which motivated to include this appendix. Two alternative derivations are presented; first, starting from the N-S equations in a rotating frame; second, starting from an inertial frame. The notations used are the same as in the main text.

1 Starting from the N-S equations of fluid flow in a rotating frame [25,26].

a Conservation of Mass

$$\left[\frac{\partial \rho}{\partial t} \right]_r + \nabla \cdot \rho \mathbf{u}_r = 0 \quad (\text{A1.1})$$

Substituting $\mathbf{u}_r = \mathbf{u}_{in} - \boldsymbol{\Omega} \times \mathbf{r}$ yields

$$\begin{aligned} \left[\frac{\partial \rho}{\partial t} \right]_r + \nabla \cdot \rho \mathbf{u}_{in} - \nabla \cdot \rho (\boldsymbol{\Omega} \times \mathbf{r}) &= \\ \left[\frac{\partial \rho}{\partial t} \right]_r + \nabla \cdot \rho \mathbf{u}_{in} - \underbrace{\rho \nabla \cdot (\boldsymbol{\Omega} \times \mathbf{r})}_{=0} - (\nabla \rho) \cdot (\boldsymbol{\Omega} \times \mathbf{r}) &= \\ \left[\frac{\partial \rho}{\partial t} \right]_r + \nabla \cdot \rho \mathbf{u}_{in} - \underbrace{(\boldsymbol{\Omega} \times \mathbf{r}) \cdot \nabla \rho}_{\text{rot. advection of density}} &= 0. \end{aligned} \quad (\text{A1.2})$$

a Conservation of Momentum

$$\rho \left[\frac{\partial \mathbf{u}_r}{\partial t} \right]_r + \rho \mathbf{u}_r \cdot \nabla \mathbf{u}_r = \nabla \cdot \boldsymbol{\sigma}_{in} + \underbrace{\mathbf{F}_{in} - 2\rho \boldsymbol{\Omega} \times \mathbf{u}_r}_{\text{Coriolis force}} - \underbrace{\rho \boldsymbol{\Omega} \times (\boldsymbol{\Omega} \times \mathbf{r})}_{\text{Centrifugal force}} \quad (\text{A1.3})$$

Substituting $\mathbf{u}_r = \mathbf{u}_{in} - \boldsymbol{\Omega} \times \mathbf{r}$, noting that $\frac{\partial \boldsymbol{\Omega} \times \mathbf{r}}{\partial t} = 0$ (time-constant rotation) $\mathbf{F}_{in} = \mathbf{F}_r$ yields

$$\rho \left[\frac{\partial \mathbf{u}_{in}}{\partial t} \right]_r + \rho (\mathbf{u}_{in} - \boldsymbol{\Omega} \times \mathbf{r}) \cdot \nabla (\mathbf{u}_{in} - \boldsymbol{\Omega} \times \mathbf{r}) = \nabla \cdot \boldsymbol{\sigma}_r + \mathbf{F}_r - 2\rho \boldsymbol{\Omega} \times \mathbf{u}_{in} + \rho \boldsymbol{\Omega} \times (\boldsymbol{\Omega} \times \mathbf{r})$$

Rearranging

$$\begin{aligned} (\mathbf{u}_{in} - \boldsymbol{\Omega} \times \mathbf{r}) \cdot \nabla (\mathbf{u}_{in} - \boldsymbol{\Omega} \times \mathbf{r}) \\ \mathbf{u}_{in} \cdot \nabla \mathbf{u}_{in} - \underbrace{\mathbf{u}_{in} \cdot \nabla (\boldsymbol{\Omega} \times \mathbf{r})}_{\boldsymbol{\Omega} \times \mathbf{u}_{in}} + \underbrace{(\boldsymbol{\Omega} \times \mathbf{r}) \cdot \nabla (\boldsymbol{\Omega} \times \mathbf{r})}_{\boldsymbol{\Omega} \times (\boldsymbol{\Omega} \times \mathbf{r})} - (\boldsymbol{\Omega} \times \mathbf{r}) \cdot \nabla \mathbf{u}_{in} = \\ \mathbf{u}_{in} \cdot \nabla \mathbf{u}_{in} - (\boldsymbol{\Omega} \times \mathbf{u}_{in}) + \boldsymbol{\Omega} \times (\boldsymbol{\Omega} \times \mathbf{r}) - (\boldsymbol{\Omega} \times \mathbf{r}) \cdot \nabla \mathbf{u}_{in} \end{aligned}$$

Leads to

$$\rho \left[\frac{\partial \mathbf{u}_{in}}{\partial t} \right]_r + \rho \mathbf{u}_{in} \cdot \nabla \mathbf{u}_{in} - \rho (\boldsymbol{\Omega} \times \mathbf{r}) \cdot \nabla \mathbf{u}_{in} = \nabla \cdot \boldsymbol{\sigma}_r + \mathbf{F}_r - \rho \boldsymbol{\Omega} \times \mathbf{u}_{in}$$

The internal stress tensor reads

$$\begin{aligned} \boldsymbol{\sigma}_r &= -p \mathbf{I} + \mu (\nabla \mathbf{u}_r + (\nabla \mathbf{u}_r)^T) + \left(\mu_b - \frac{2}{3} \mu \right) (\nabla \cdot \mathbf{u}_r) \mathbf{I} = \\ &= -p \mathbf{I} + \mu (\nabla (\mathbf{u}_{in} - \boldsymbol{\Omega} \times \mathbf{r}) + (\nabla (\mathbf{u}_{in} - \boldsymbol{\Omega} \times \mathbf{r}))^T) + \left(\mu_b - \frac{2}{3} \mu \right) (\nabla \cdot (\mathbf{u}_{in} - \boldsymbol{\Omega} \times \mathbf{r})) \mathbf{I} \end{aligned}$$

Noting that $\nabla (\boldsymbol{\Omega} \times \mathbf{r}) + \nabla (\boldsymbol{\Omega} \times \mathbf{r})^T = 0$ and $\nabla \cdot (\boldsymbol{\Omega} \times \mathbf{r}) = 0$ leads to

$$\boldsymbol{\sigma}_r = \boldsymbol{\sigma}_{in}$$

And therefore

$$\rho \left[\frac{\partial \mathbf{u}_{in}}{\partial t} \right]_r + \rho \mathbf{u}_{in} \cdot \nabla \mathbf{u}_{in} \underbrace{- \rho (\boldsymbol{\Omega} \times \mathbf{r}) \cdot \nabla \mathbf{u}_{in}}_{\text{rot. advection of momentum}} = \nabla \cdot \boldsymbol{\sigma}_{in} + \mathbf{F}_r \underbrace{- \rho \boldsymbol{\Omega} \times \mathbf{u}_{in}}_{\text{Coriolis force related term}} \quad (\text{A1.4})$$

a Conservation of Energy

$$\rho T \left[\frac{\partial s}{\partial t} \right]_r + \rho T \mathbf{u}_r \cdot \nabla s = \nabla \cdot k \nabla T + \varnothing_r + S_h \quad (\text{A1.5})$$

and $\rho T ds = \rho c_p dT - \alpha_p T dp$.

Substituting $\mathbf{u}_r = \mathbf{u}_{in} - \boldsymbol{\Omega} \times \mathbf{r}$

And noting that $\nabla (\boldsymbol{\Omega} \times \mathbf{r}) = 0$ and $\boldsymbol{\tau}_r = \boldsymbol{\tau}_{in}$ yields

$$\varnothing_r = \nabla \mathbf{u}_r : \boldsymbol{\tau}_r = \nabla \mathbf{u}_{in} : \boldsymbol{\tau}_{in} = \varnothing_{in}$$

And

$$\rho T \left[\frac{\partial s}{\partial t} \right]_r + \rho T \mathbf{u}_{in} \cdot \nabla s \underbrace{- \rho T (\boldsymbol{\Omega} \times \mathbf{r}) \cdot \nabla s}_{\text{rot. advection of entropy}} = \nabla \cdot k \nabla T + \varnothing_{in} + S_h. \quad (\text{A1.6})$$

1 Starting from the N-S equations of fluid flow in an inertial frame

Starting point are the equations of fluid flow expressed in absolute time derivatives [48]

$$\left\{ \begin{array}{l} \left[\frac{D\rho}{Dt} \right]_{in} + \rho \nabla \cdot \mathbf{u}_{in} = 0 \\ \rho \left[\frac{D\mathbf{u}_{in}}{Dt} \right]_{in} = \nabla \cdot \boldsymbol{\sigma}_{in} + \mathbf{F}_r \\ \rho T \left[\frac{Ds}{Dt} \right]_{in} = \nabla \cdot k \nabla T + \phi_{in} + S_h \end{array} \right. \quad (\text{A2.1})$$

Note that the external source terms \mathbf{F}_r and S_h as well as ϕ_{in} are independent of if they are calculated in the inertial or relative frame. The next step is to use the relationship between absolute time derivatives in the inertial and relative frames [24,47]:

$$\left\{ \begin{array}{l} \left[\frac{Dq}{Dt} \right]_{in} = \left[\frac{Dq}{Dt} \right]_r, \text{ for any scalar field } q \\ \left[\frac{D\mathbf{a}}{Dt} \right]_{in} = \left[\frac{D\mathbf{a}}{Dt} \right]_r + \boldsymbol{\Omega} \times \mathbf{a}, \text{ for any vector field } \mathbf{a} \end{array} \right. \quad (\text{A2.2})$$

The absolute time derivatives in the relative frame are given by

$$\begin{cases} \left[\frac{Dq}{Dt} \right]_{\mathbf{r}} = \left[\frac{\partial q}{\partial t} \right]_{\mathbf{r}} + \mathbf{u}_{\mathbf{r}} \cdot \nabla q = \left[\frac{\partial q}{\partial t} \right]_{\mathbf{r}} + (\mathbf{u}_{\text{in}} - \boldsymbol{\Omega} \times \mathbf{r}) \cdot \nabla q \\ \left[\frac{D\mathbf{a}}{Dt} \right]_{\mathbf{r}} = \left[\frac{\partial \mathbf{a}}{\partial t} \right]_{\mathbf{r}} + \mathbf{u}_{\mathbf{r}} \cdot \nabla \mathbf{a} = \left[\frac{\partial \mathbf{a}}{\partial t} \right]_{\mathbf{r}} + (\mathbf{u}_{\text{in}} - \boldsymbol{\Omega} \times \mathbf{r}) \cdot \nabla \mathbf{a} \end{cases} \quad (\text{A2.3})$$

Using these last results in Eq. (A2.1) gives

$$\begin{cases} \left[\frac{\partial \rho}{\partial t} \right]_{\mathbf{r}} + (\mathbf{u}_{\text{in}} - \boldsymbol{\Omega} \times \mathbf{r}) \cdot \nabla \rho + \rho \nabla \cdot \mathbf{u}_{\text{in}} = 0 \\ \rho \left(\left[\frac{\partial \mathbf{u}_{\text{in}}}{\partial t} \right]_{\mathbf{r}} + (\mathbf{u}_{\text{in}} - \boldsymbol{\Omega} \times \mathbf{r}) \cdot \nabla \mathbf{u}_{\text{in}} + \boldsymbol{\Omega} \times \mathbf{u}_{\text{in}} \right) = \nabla \cdot \boldsymbol{\sigma}_{\text{in}} + \mathbf{F}_{\mathbf{r}}, \\ \rho T \left(\left[\frac{\partial s}{\partial t} \right]_{\mathbf{r}} + (\mathbf{u}_{\text{in}} - \boldsymbol{\Omega} \times \mathbf{r}) \cdot \nabla s \right) = \nabla \cdot k \nabla T + \phi_{\text{in}} + S_{\text{h}} \end{cases} \quad (\text{A2.4})$$

which can be written as

$$\begin{cases} \left[\frac{\partial \rho}{\partial t} \right]_{\mathbf{r}} + \nabla \cdot \rho \mathbf{u}_{\text{in}} - (\boldsymbol{\Omega} \times \mathbf{r}) \cdot \nabla \rho = 0 \\ \rho \left[\frac{\partial \mathbf{u}_{\text{in}}}{\partial t} \right]_{\mathbf{r}} + \rho \mathbf{u}_{\text{in}} \cdot \nabla \mathbf{u}_{\text{in}} - \rho (\boldsymbol{\Omega} \times \mathbf{r}) \cdot \nabla \mathbf{u}_{\text{in}} = \nabla \cdot \boldsymbol{\sigma}_{\text{in}} + \mathbf{F}_{\mathbf{r}} - \rho \boldsymbol{\Omega} \times \mathbf{u}_{\text{in}} \\ \rho T \left[\frac{\partial s}{\partial t} \right]_{\mathbf{r}} + \rho T \mathbf{u}_{\text{in}} \cdot \nabla s - \rho T (\boldsymbol{\Omega} \times \mathbf{r}) \cdot \nabla s = \nabla \cdot k \nabla T + \phi_{\text{in}} + S_{\text{h}} \end{cases} \quad (\text{A2.5})$$

References

- [1] M.S. Howe, *Acoustics of Fluid-Structure Interactions*, Cambridge Univ. Press, Cambridge, UK, 1998.
- [2] T. Emmert, S. Bomberg, W. Polifke, Intrinsic thermoacoustic instability of premixed flames, *Combust. Flame* 162 (1) (2015) 75–85, <https://doi.org/10.1016/j.combustflame.2014.06.008>.
- [3] A. Kierkegaard, S. Allam, G. Efraimsson, M. Åbom, Simulations of whistling and the whistling potentiality of an in-duct orifice with linear aeroacoustics, *J. Sound Vib.* 331 (5) (2012) 1084–1096, <https://doi.org/10.1016/j.jsv.2011.10.028>.
- [4] C. Soward, Y. Aurégan, W. Polifke, Parametric LES/SI Based Aeroacoustic Characterization of Tandem Orifices in Low Mach Number Flows, *Acta Acust. united with Acust.* 102 (5) (2016).
- [5] S. Bouley, B. François, M. Roger, H. Posson, S. Moreau, On a two-dimensional mode-matching technique for sound generation and transmission in axial-flow outlet guide vanes, *J. Sound Vib.* 403 (2017) 190–213, <https://doi.org/10.1016/j.jsv.2017.04.031>.
- [6] R.B. Navarro and R. Corral, “Efficient Fan Broadband Noise Prediction Using Navier-Stokes Linearized Analysis,” in 25th AIAA/CEAS Aeroacoustics Conference, Delf, The Netherlands, doi: 10.2514/6.2019-2624.
- [7] A. Bissuel, G. Allaire, L. Daumas, S. Barré, F. Rey, Linearized Navier–Stokes equations for aeroacoustics using stabilized finite elements: boundary conditions and industrial application to aft-fan noise propagation, *Comput. Fluids* 166 (2018) 32–45, <https://doi.org/10.1016/j.compfluid.2018.01.011>.
- [8] W. Ullrich, et al., Combustion Noise Prediction Using Linearized Navier–Stokes Equations and Large-Eddy Simulation Sources, *J. Propuls. Power* 34 (2017), <https://doi.org/10.2514/1.B36428>.
- [9] A. Onorati, G. Montenegro, 1D and Multi-D Modeling Techniques for IC Engine Simulation, in: *1D and Multi-D Modeling Techniques for IC Engine Simulation*, SAE, 2020 pp. i–xix.
- [10] S. Sharma, J. García-Tiscar, J.M. Allport, S. Barrans, A.K. Nickson, Evaluation of modelling parameters for computing flow-induced noise in a small high-speed centrifugal compressor, *Aerosp. Sci. Technol.* 98 (2020), 105697, <https://doi.org/10.1016/j.ast.2020.105697>.
- [11] E. Sundström, B. Semlitsch, M. Mihaescu, Acoustic signature of flow instabilities in radial compressors, *J. Sound Vib.* 434 (Nov. 2018) 221–236, <https://doi.org/10.1016/j.jsv.2018.07.040>.
- [12] E. Sundström, B. Semlitsch, M. Mihaescu, Generation Mechanisms of Rotating Stall and Surge in Centrifugal Compressors, *Flow Turbul. Combust.* 100 (Apr. 2018) 705–719, <https://doi.org/10.1007/s10494-017-9877-z>.
- [13] E. Casartelli, L. Mangani, D. Roos Launchbury, A. Del Rio, Application of Advanced RANS Turbulence Models for the Prediction of Turbomachinery Flows, *J. Turbomach.* 144 (1) (2021), <https://doi.org/10.1115/1.4051938>.
- [14] R.B. Veloso, Y. Elneer, F.M. Reich, S. Allam, Simulation of sound transmission through automotive turbochargers, in: 7th International Styrian Noise, Vibration & Harshness Congress: The European Automotive Noise Conference, Graz, Austria, 2012, <https://doi.org/10.4271/2012-01-1560>.
- [15] K.S. Peat, A.J. Torregrosa, A. Broatch, T. Fernández, An investigation into the passive acoustic effect of the turbine in an automotive turbocharger, *J. Sound Vib.* 295 (1) (2006) 60–75, <https://doi.org/10.1016/j.jsv.2005.11.033>.
- [16] C. Foulquié, S. Khelladi, M. Deligant, L. Ramírez, X. Nogueira, J. Mardjono, Numerical assessment of fan blades screen effect on fan/OGV interaction tonal noise, *J. Sound Vib.* 481 (2020), 115428, <https://doi.org/10.1016/j.jsv.2020.115428>.
- [17] E. Vargas Loureiro, et al., Evaluation of low fidelity and CFD methods for the aerodynamic performance of a small propeller, *Aerosp. Sci. Technol.* 108 (2021), 106402, <https://doi.org/10.1016/j.ast.2020.106402>.
- [18] M.B. Dogruoz, G. Shankaran, Computations with the multiple reference frame technique: flow and temperature fields downstream of an axial fan, *Numer. Heat Transf. Part A Appl.* 71 (5) (Mar. 2017) 488–510, <https://doi.org/10.1080/10407782.2016.1277930>.
- [19] R. Franzke, S. Sebben, T. Bark, E. Willeon, A. Broniewicz, Evaluation of the Multiple Reference Frame Approach for the Modelling of an Axial Cooling Fan, *Energies* 12 (2019) 2934, <https://doi.org/10.3390/en12152934>.
- [20] J. Liu, H. Lin, S.R. Purimilla, Wake field studies of tidal current turbines with different numerical methods, *Ocean Eng* 117 (2016) 383–397, <https://doi.org/10.1016/j.oceaneng.2016.03.061>.
- [21] M. Åbom, Measurement of the scattering-matrix of acoustical two-ports, *Mech. Syst. Signal Process.* 5 (2) (1991) 89–104, [https://doi.org/10.1016/0888-3270\(91\)90017-Y](https://doi.org/10.1016/0888-3270(91)90017-Y).

- [22] R. Kabral, M. Åbom, Investigation of turbocharger compressor surge inception by means of an acoustic two-port model, *J. Sound Vib.* 412 (2018) 270–286, <https://doi.org/10.1016/j.jsv.2017.10.003>.
- [23] ANSYS Inc., Ansys® Fluent 15 Theory Guide - 2.2.1 Equations for a Rotating Reference Frame (enea.it, online Aug 2022): <https://www.afs.enea.it/project/neptunius/docs/fluent/html/th/node30.htm#sec-rotate-equations>.
- [24] “OpenFoam Implementation Reference (online Aug. 2022).” https://openfoamwiki.net/index.php/See_the_MRF_development.
- [25] C. Hirsch, *Numerical Computation of Internal & External Flows: Fundamentals of Numerical Discretization*. 605 Third Ave, John Wiley & Sons, Inc., New York, NY, United States, 1988.
- [26] M.L. Combrinck, L.N. Dala, I.I. Lipatov, Eulerian derivation of non-inertial Navier–Stokes and boundary layer equations for incompressible flow in constant pure rotation, *Eur. J. Mech. - B/Fluids* 65 (2017) 10–30, <https://doi.org/10.1016/j.euromechflu.2016.12.012>.
- [27] M.L. Munjal, *Acoustics of Ducts and Mufflers*, 2nd ed., John Wiley & Sons, New York, NY, 2014.
- [28] M. Shur, et al., Experimental/numerical study of ducted-fan noise: effect of duct inlet shape, *AIAA J* 56 (3) (Mar. 2018) 979–996, <https://doi.org/10.2514/1.J055870>.
- [29] S.V. Lympny and K.K. Ahuja, “An Experimental Facility for Measuring the Acoustic Reflection and Transmission of Higher-Order Modes in Heated Flows, Part 2: experiments and Analysis,” doi: 10.2514/6.2018-3134.
- [30] A. Snakowska, J. Jurkiewicz, A new approach to the theory of acoustic multi-port networks with multimode wave and its application to muffler analysis, *J. Sound Vib.* 490 (2021), 115722, <https://doi.org/10.1016/j.jsv.2020.115722>.
- [31] I. R., G.D. Luo JY, Prediction of impeller induced flows in mixing vessels using multiple frames of reference, *The Institution of Chemical Engineers* (1994) 549–555, pp. 549–556.
- [32] S. Sack, M. Åbom, G. Efrimsson, On acoustic multi-port characterisation including higher order modes, *Acta Acust. united with Acust.* 102 (5) (2016) 834–850, <https://doi.org/10.3813/AAA.918998>.
- [33] S. Sack, M. Shur, M. Åbom, M. Strelets, A. Travin, Numerical eduction of active multi-port data for in-duct obstructions, *J. Sound Vib.* 411 (2017) 328–345, <https://doi.org/10.1016/j.jsv.2017.09.012>.
- [34] C. Weng, S. Boij, A. Hanifi, On the calculation of the complex wavenumber of plane waves in rigid-walled low-Mach-number turbulent pipe flows, *J. Sound Vib.* 354 (2015) 132–153, <https://doi.org/10.1016/j.jsv.2015.06.013>.
- [35] E. Dokumaci, On the effect of viscosity and thermal conductivity on sound propagation in ducts: a re-visit to the classical theory with extensions for higher order modes and presence of mean flow, *J. Sound Vib.* 333 (21) (2014) 5583–5599, <https://doi.org/10.1016/j.jsv.2014.06.007>.
- [36] C. Weng, F. Bake, An analytical model for boundary layer attenuation of acoustic modes in rigid circular ducts with uniform flow, *Acta Acust. united with Acust.* 102 (6) (2016) 1138–1141, <https://doi.org/10.3813/AAA.919025>.
- [37] E.H. Moore, On the reciprocal of the general algebraic matrix, *Bull. Am. Math. Soc.* 26 (1920) 394–395.
- [38] F.R. Menter, Two-equation eddy-viscosity turbulence models for engineering applications, *AIAA J* 32 (8) (1994) 1598–1605, <https://doi.org/10.2514/3.12149>.
- [39] E. Sundström, B. Semlitsch, M. Mihaescu, Assessment of the 3D Flow in a Centrifugal Compressor Using Steady-State and Unsteady Flow Solvers, in: *SAE Technical Papers* 2014, 2014, <https://doi.org/10.4271/2014-01-2856>.
- [40] “COMSOL Multiphysics®, v. 5.5.” COMSOL AB, Stockholm, Sweden, [Online]. Available: www.comsol.com.
- [41] P.R. Amestoy, I.S. Duff, J. Koster, J.-Y. L'Excellent, A Fully Asynchronous Multifrontal Solver Using Distributed Dynamic Scheduling, *SIAM J. Matrix Anal. Appl.* 23 (1) (2001) 15–41.
- [42] P.R. Amestoy, A. Buttari, J.-Y. L'Excellent, T. Mary, Performance and Scalability of the Block Low-Rank Multifrontal Factorization on Multicore Architectures, *ACM Trans. Math. Softw.* 45 (1) (2019), pp. 2:1–2:26.
- [43] S. Sack, acdecom—A Python module for acoustic wave decomposition in flow ducts, *Softw. Impacts* 6 (2020), 100025, <https://doi.org/10.1016/j.simpa.2020.100025>.
- [44] E.C. Levy, Complex-curve fitting, *IRE Trans. Autom. Control* AC-4 (1) (1959) 37–43, <https://doi.org/10.1109/TAC.1959.6429401>.
- [45] M. Åbom, R. Kabral, Turbocharger Noise - Generation and Control, in: *SAE Technical Paper*, 2014, <https://doi.org/10.4271/2014-36-0802>.
- [46] D.G. Holmes, S.S. Tong, A Three-Dimensional Euler Solver for Turbomachinery Blade Rows, *J. Eng. Gas Turbines Power* 107 (2) (Apr. 1985) 258–264, <https://doi.org/10.1115/1.3239705>.
- [47] F. Cariglino, PhD Thesis, Polytechnic of Turin, 2013, <https://doi.org/10.6092/polito/porto/2573563>.
- [48] G.K. Batchelor, *An Introduction to Fluid Dynamics*, Cambridge University Press, Cambridge, 2000.